Nano Research

Open Access

Research Article

A nanoflower-on-nanowire heterogeneous electrocatalyst for enhanced interfacial water activation in nitrate reduction reaction

Jingwen Yu[1], Yunliang Liu[1], Cunhao Fan[1], Naiyun Liu[1] ✉, Jingya Yin[2], Yaxi Li[1], Yuanyuan Cheng[1], Xinya Yuan[1], Xinyue Zhang[1], Yixian Liu[1], Sanjun Fan[3] ✉, Lei Xu[4,5] ✉, and Haitao Li[1] ✉

[1] *Institute for Energy Research, School of Chemistry and Chemical Engineering, Jiangsu University, Zhenjiang 212013, China*
[2] *Qingdao Municipal Center for Disease Control and Prevention, Qingdao 266033, China*
[3] *Department of Chemistry and Biochemistry, The Ohio State University, Columbus, Ohio 43210, USA*
[4] *Jiangsu Engineering Technology Research Center of Biomass Composites and Addictive Manufacturing, Institute of Agricultural Facilities and Equipment, Jiangsu Academy of Agricultural Sciences, Nanjing 210014, China*
[5] *Key Laboratory for Protected Agricultural Engineering in the Middle and Lower Reaches of Yangtze River, Ministry of Agriculture and Rural Affairs, Nanjing 210014, China*

Cite this article: *Nano Research*, **2025**, *18*, 94907135. https://doi.org/10.26599/NR.2025.94907135

ABSTRACT: Electrocatalytic nitrate reduction reaction (NitRR) is an efficient route for simultaneous wastewater treatment and ammonia production, but the conversion of NO_3^- to NH_3 involves multiple electron and proton transfer processes and diverse by-products. Therefore, developing ammonia catalysts with superior catalytic activity and selectivity is an urgent task. The distinctive electronic structure of Cu enhances the adsorption of nitrogen-containing intermediates, but the insufficient activation capability of Cu for interfacial water restricts the generation of reactive hydrogen and inhibits the hydrogenation process. In this work, a Ce-doped CuO catalyst (Ce_{10}/CuO) was synthesized by *in situ* oxidative etching and annealing. The redox of Ce^{3+}/Ce^{4+} enables the optimization of the electronic structure of the catalyst, and the presence of Ce^{3+} as a defect indicator introduces more oxygen vacancies. The results demonstrate that Ce_{10}/CuO provides an impressive ammonia yield of 3.88 ± 0.14 mmol·cm^{-2}·h^{-1} at 0.4 V vs. reversible hydrogen electrode (RHE) with an increase of 1.04 mmol·cm^{-2}·h^{-1} compared to that of pure CuO, and the Faradaic efficiencies (FE) reaches 93.2% ± 3.4%. *In situ* characterization confirms the doping of Ce facilitates the activation and dissociation of interfacial water, which promotes the production of active hydrogen and thus enhances the ammonia production efficiency.

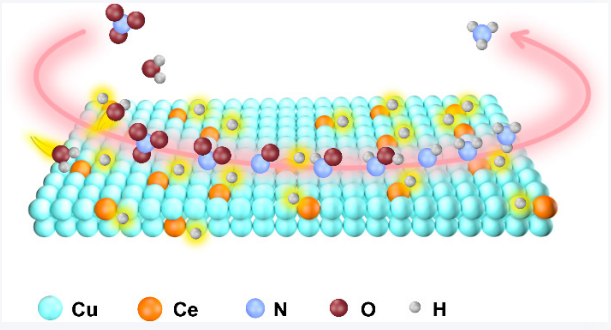

KEYWORDS: active hydrogen, electron transfer, nitrate, ammonia

1 Introduction

Ammonia (NH_3) is a critical raw material for industrial and agricultural production which urgently requires a scalable and sustainable ammonia production process [1–11]. However, the Haber–Bosch method with high energy consumption and harsh process conditions still dominates the current industrial-scale production, and the massive carbon dioxide emission during production exacerbates the environmental problems [12–17]. Electrochemical production has attracted extensive research based on the low cost, energy conservation, and high efficiency [18–27]. The electrocatalytic nitrogen reduction reaction (NRR) is hindered by the stable N≡N bond and the low solubility of nitrogen in water, which accompanies severe competition for hydrogen evolution reaction (HER) during the reduction process [28–31].

Nitrate as a substitution for nitrogen presents the following advantages: (1) The bond energy of the N=O bond (204 kJ·mol^{-1}) is considerably lower than that of the N≡N bond (941 kJ·mol^{-1}), which greatly decreases the reaction energy barrier [32–34]. (2) Nitrate (880 g·L^{-1}) is more soluble than nitrogen (0.02 g·L^{-1}) in water, avoiding complex gas–liquid–solid interface interactions [35–38]. (3) The overuse and emission of nitrate in agriculture and

Received: October 23, 2024; **Revised:** November 9, 2024
Accepted: November 12, 2024

✉Address correspondence to Naiyun Liu, liuny@ujs.edu.cn; Sanjun Fan, fan.1113@osu.com; Lei Xu, xulei@jaas.ac.cn; Haitao Li, liht@ujs.edu.cn

industry pose a serious threat to the ecosystem, and the synthesis of ammonia from nitrate contributes to the elimination of nitrate pollution [39–42]. However, electrocatalytic nitrate reduction reaction (NitRR) to ammonia ($NO_3^- + 6H_2O + 8e^- \rightarrow NH_3 + 9OH^-$) is a kinetically sluggish eight-electron transfer process and involves multiple reaction intermediates (NO_2^-, NO, NH_2OH, NH_2, etc.), which is a tremendous challenge for the design of catalysts [43, 44].

Noble metals including Pd, Rh, and Ru have already been applied for NitRR, however, the scarcity and high price of these metals dramatically limit their large-scale industrial production [45–51]. The Cu-based material represents one of the most effective and economical metal catalysts for the conversion of nitrate to ammonia with high conversion efficiency under ambient conditions [52–56]. Cu tends to transfer electrons to the lowest unoccupied molecular orbital (π^* orbital) of the nitrate [57, 58]. The unique electronic structure of Cu can enhance the adsorption of nitrogen-containing intermediates during the reduction of nitrate to ammonia, which results in a continuum in the whole process of reduction [59]. However, Cu is not sufficiently activated for interfacial water, which restricts the generation of active hydrogen and thus inhibits the hydrogenation process [28, 60]. The effectiveness of metal doping in nitrate reduction has previously been proven. It has been reported that the introduction of metals such as Ru, Pd, Rh, Fe, Co, and Ni is effective in promoting the catalytic performance of Cu through electronic and strain effects [61–66]. However, the construction of bimetallic catalysts with rare earth elements and Cu for electrocatalytic nitrate reduction is still relatively uncommon. Cerium (Ce) is the most abundant and least expensive of the rare earth elements. It possesses an incompletely filled 4f orbital and a relatively low electronegativity. The redox of Ce^{3+}/Ce^{4+} can be performed by trapping and activating oxygen molecules and generating numerous oxygen vacancies, which modulates the electronic structure of Cu-based catalysts as well as the adsorption capacity of intermediates.

In this work, Ce-doped CuO (Ce_{10}/CuO) was prepared by *in situ* oxidative etching and annealing and applied for the electrocatalytic nitrate reduction to ammonia. The doping of Ce enables the emergence of more oxygen vacancies and optimizes the electronic structure of the catalyst, which facilitates the adsorption of NO_2^-. In addition, the introduction of Ce can strengthen the activation and dissociation of interfacial water and generate more active hydrogen, which contributes to the hydrogenation of nitrogen-containing intermediates during the nitrate reduction process. The ammonia yield of Ce_{10}/CuO attains 3.88 ± 0.14 mmol·cm^{-2}·h^{-1} at –0.4 V vs. reversible hydrogen electrode (RHE) with an increase of 1.04 mmol·cm^{-2}·h^{-1} compared to that of CuO, and the FE of NH_3 is up to 93.2% ± 3.4%. Furthermore, the Zn-NO_3^- battery was successfully assembled with a peak power density of 14.5 mW·cm^{-2} at 38 mA·cm^{-2} and a FE of 98.4% for NH_3 at 40 mA·cm^{-2}, which exceeds most of the reported catalysts.

2 Experimental

2.1 Reagents and chemicals

All materials such as cerium nitrate hexahydrate ($Ce(NO_3)_3·6H_2O$), sodium hydroxide (NaOH), ammonium persulfate ($(NH_4)_2S_2O_8$), hydrochloric acid (HCl), potassium hydroxide (KOH), potassium nitrate (KNO_3), ethanol (C_2H_6O) were analytical grade reagents and purchased from Sigma Aldrich and Sinopharm. All reagents and chemicals were used as received without further purification.

2.2 Synthesis of CuO

Typically, CuO nanowires were synthesized by calcinating treatment of the *in situ*-grown $Cu(OH)_2$ nanowires on copper foam. First, the copper foam was ultrasonically cleaned in 3 M hydrochloric acid, ethanol, and deionized water for 10 min. 2.5 mmol $(NH_4)_2S_2O_8$ was added to 20 mL 2.5 mM NaOH solution to form a homogeneous mixed solution. After that, the cleaned copper foam was immersed into the mixed solution and kept for 20 min. The samples were rinsed with deionized water and ethanol three times, then dried under vacuum for 6 h. The as-made blue $Cu(OH)_2$ nanowires were placed in a muffle furnace and then calcined at 200 °C for 1 h to obtain dark brown CuO nanowires grown on copper foam.

2.3 Synthesis of Ce/CuO

The prepared self-supported $Cu(OH)_2$ nanowires were impregnated into 0.25, 0.5, 1, 2.5, 5, 10, 20, 40, 60, and 80 mM aqueous solution of $Ce(NO_3)_3·6H_2O$ for 1 h, and then calcinated at 200 °C for 1 h, respectively. The obtained $Ce_{0.25}$/CuO, $Ce_{0.5}$/CuO, Ce_1/CuO, $Ce_{2.5}$/CuO, Ce_5/CuO, Ce_{10}/CuO, Ce_{20}/CuO, Ce_{40}/CuO, and Ce_{60}/CuO could be used for subsequent characterization and testing.

3 Results and discussion

A schematic of the process for synthesizing Ce_{10}/CuO is shown in Fig. 1(a). $Cu(OH)_2$ nanowires were initially *in situ* grown on a smooth copper foam surface by oxidative etching. The resulting $Cu(OH)_2$ was subsequently impregnated in $Ce(NO_3)_3·6H_2O$ solution and then calcined to obtain Ce/CuO. Cu^{2+} and OH^- on the catalyst surface diffused outward under a concentration gradient and were trapped in the interstitial spaces of the nanowires. Simultaneously, Ce^{3+} also diffused into the interstitial space and surface of the nanowires due to the concentration difference. The Cu^{2+} and OH^- retained in the interstitial space of the nanowires gradually formed $Cu(OH)_2$ nanosheets in the subsequent annealing process. The Ce^{3+} was successfully doped to the $Cu(OH)_2$ nanowires and $Cu(OH)_2$ nanosheets throughout the process due to its diffusion. The scanning electron microscopy (SEM) images of CuO and Ce_{10}/CuO show vertically and homogeneously grown nanowire arrays on the smooth Cu foam surface (Fig. 1(b) and Fig. S1 in the Electronic Supplementary Material (ESM)). In contrast, Ce_{10}/CuO exhibits a massive distribution of spherical structures made of stacked nanosheets in the nanowire arrays (Figs. 1(c) and 1(d)). Energy dispersive X-ray (EDX) spectrum and elemental mapping analysis reveal that Ce, Cu, and O are the basic elements in Ce_{10}/CuO and confirm the uniform distribution of Ce, Cu, and O on Ce_{10}/CuO (Fig. 1(e) and Figs. S2 and S3 in the ESM).

Furthermore, the specific components and structure of the catalysts can be analyzed by high-resolution transmission electron microscopy (HRTEM) images, X-ray diffraction (XRD) spectra, and X-ray photoelectron spectroscopy (XPS). The HRTEM image of Ce_{10}/CuO reveals the characteristic crystalline spacing of 0.250 nm attributed to the $(11\bar{1})$ crystalline facets of CuO (Fig. 2(a) and Fig. S4 in the ESM). The XRD spectrum exhibits the prominent three diffraction peaks of Ce_{10}/CuO observed at 43.61°, 50.67°, and 74.29° which are attributed to the copper foam (Fig. 2(b)). The characteristic diffraction peaks at 35.60° and 38.83° corresponding to the CuO $(\bar{1}11)$ and (111) crystal planes are reflected. Diffraction peaks are observed only for CuO and Cu in Ce_{10}/CuO, suggesting that Ce ions probably replaced Cu ions relative to CuO precursors.

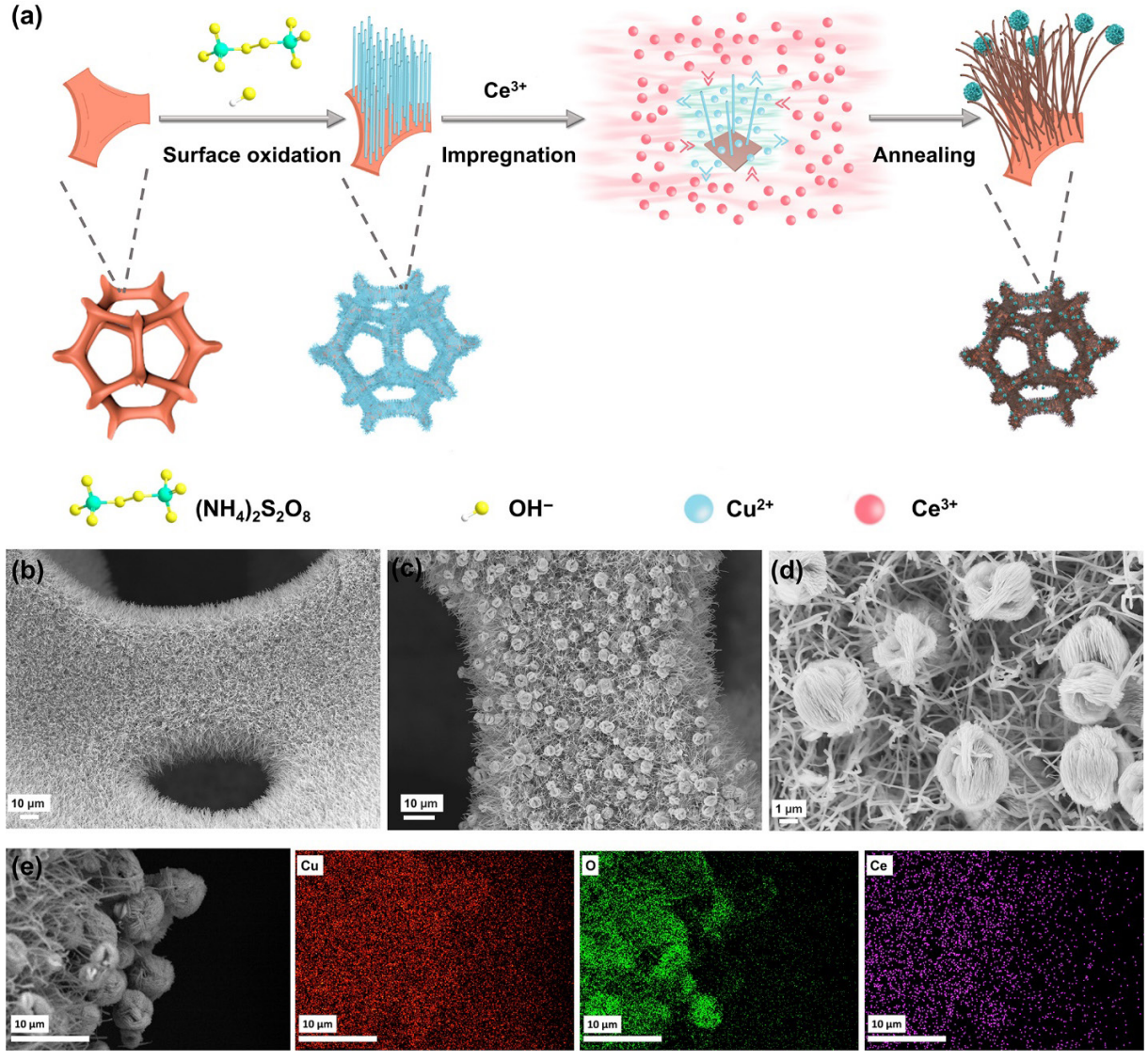

Figure 1 Synthesis and structural characterization of materials. (a) Schematic illustration for the synthesis of Ce_{10}/CuO. (b) SEM image of CuO. (c) Low-magnification and (d) high-magnification SEM images of Ce_{10}/CuO. (e) EDS mapping images of Cu, O, and Ce of Ce_{10}/CuO.

However, the low doping level during the synthesis resulted in no apparent shift of the peaks.

Fine structural characterization was carried out using XPS to probe the electronic interactions between Ce and Cu atoms on the surface of the fabricated Ce_{10}/CuO in greater depth. The full spectrum supports the presence of Cu and O elements in CuO and the additional presence of Ce in Ce_{10}/CuO (Fig. 2(c)). The high-resolution Cu 2p spectrum of CuO is deconvoluted into four peaks, i.e., Cu $2p_{3/2}$ (Cu^{2+}: 934.74 eV, Cu^{+}: 933.39 eV) and Cu $2p_{1/2}$ (Cu^{2+}: 954.33 eV, Cu^{+}: 953.11 eV) (Fig. 2(e) and Fig. S5 in the ESM). Whereas the Cu^{2+} $2p_{3/2}$, Cu^{+} $2p_{3/2}$, Cu^{2+} $2p_{1/2}$, and Cu^{+} $2p_{1/2}$ characteristic peaks of Ce_{10}/CuO are located at 934.60, 933.36, 954.33, and 952.87 eV, respectively. The miscellaneous peaks are assigned to the reorganized satellites. The Cu 2p-related characteristic peaks are shifted to lower binding energies after Ce doping. This finding demonstrates that Cu may serve as the electron acceptor and the accumulated charges lead to a possible increase in the charge density of Cu. Additionally, the high-resolution Ce 3d XPS spectrum of Ce_{10}/CuO is presented in Fig. 2(d). The characteristic peaks of the Ce oxidation state can be fitted to eight peaks [67], and u (900.88 eV), u'' (906.25 eV), u''' (916.24 eV), v (882.15 eV), v'' (887.09 eV), and v''' (898.63 eV) can be attributed to the spin-orbit double states of Ce^{4+} $3d_{5/2}$ and Ce^{4+} $3d_{3/2}$. The two peaks of Ce^{3+} species are denoted as u' (903.93 eV) and v' (885.45 eV), respectively. Accordingly, a mixture of Ce^{3+} and Ce^{4+} was introduced on the Ce_{10}/CuO surface. Moreover, the proportion of surface Ce^{3+} expressed as $Ce^{3+}/(Ce^{3+}+Ce^{4+})$ is about 40%. The presence of Ce^{3+} serving as a defect indicator promotes the generation of oxygen vacancies, remarkably. The O 1s spectrum of Ce_{10}/CuO in Fig. 2(f) is deconvoluted into lattice oxygen (O_L) at 529.56 eV, oxygen species adsorbed in the oxygen vacancies (O_V) at 531.25 eV, and oxygen species in the adsorbed water (O_A) at 532.73 eV. The O_L, O_V, and O_A peaks of CuO are located at 529.56, 531.19, and 532.66 eV, respectively. Besides, the content of O_V has increased from 47.8% to 55.6% after the introduction of Ce. The higher content of O_V may produce more active sites.

The electrochemical properties of the synthesized samples were assessed using a three-electrode H-type electrolytic cell containing 0.1 M KNO_3 and 1 M KOH. To evaluate the current density and reaction onset potential, linear scanning voltammetry (LSV) was

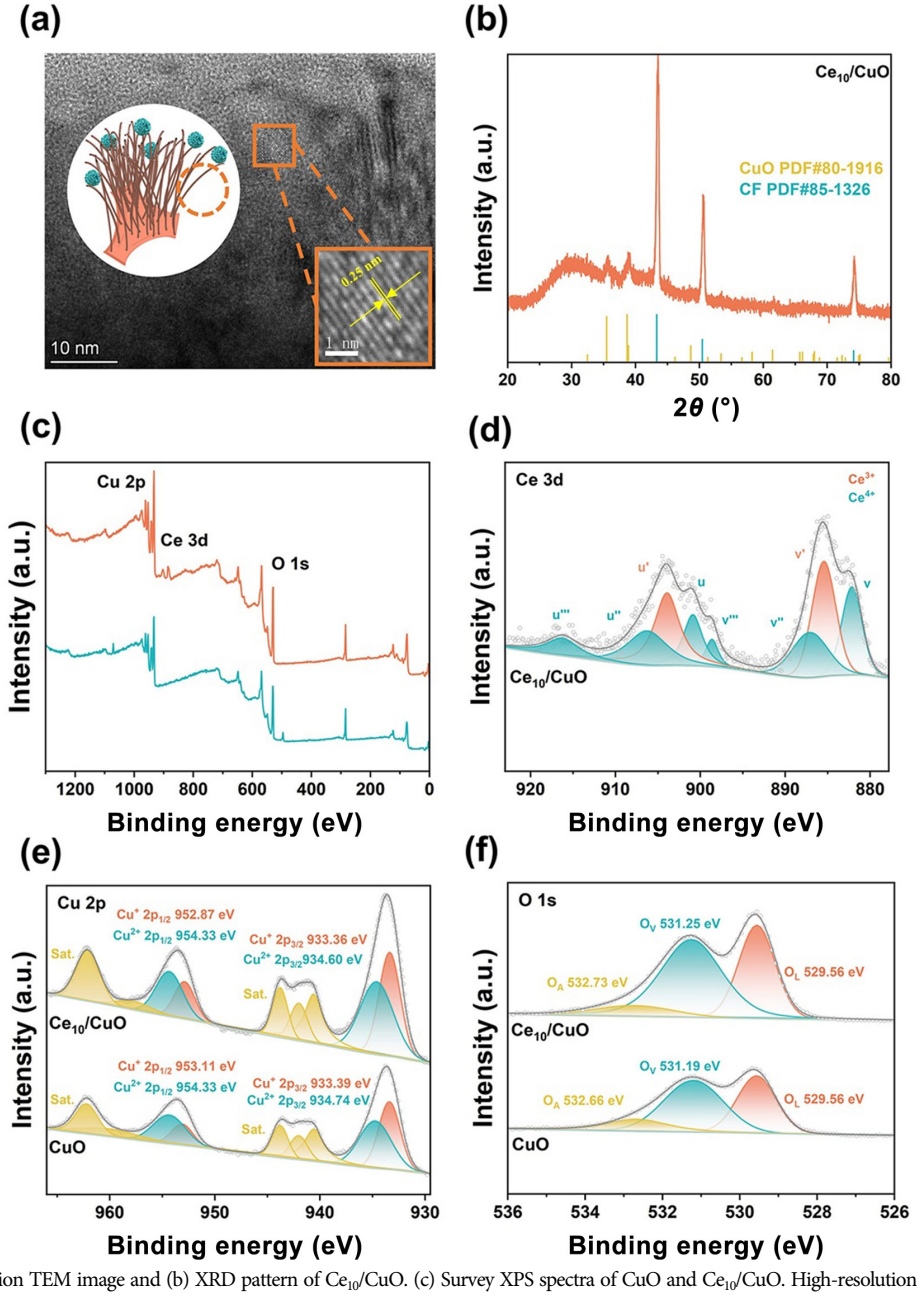

Figure 2 (a) High-resolution TEM image and (b) XRD pattern of Ce_{10}/CuO. (c) Survey XPS spectra of CuO and Ce_{10}/CuO. High-resolution XPS spectra of (d) Ce 3d, (e) Cu 2p, and (f) O 1s for as-obtained samples.

conducted. As illustrated in Fig. 3(a), the Ce_{10}/CuO has exhibited notably higher current density than CuO at the same potential. Specifically, the current density significantly increased by 0.23 A·cm^{-2} at –0.3 V vs. RHE. The enhancement indicates that the incorporation of Ce into the CuO matrix significantly improves ammonia precipitation efficiency. Moreover, the LSV curve of CuO at –0.2 V vs. RHE exhibits a clear inflection point, indicating intense competition for HER as the potential falls below –0.2 V vs. RHE. Conversely, the LSV curve of Ce_{10}/CuO shows no comparable inflection point, demonstrating that the doping of Ce promotes the reaction selectivity and charge utilization. The current density at –0.3 V vs. RHE is below 100 mA·cm^{-2} without the addition of KNO_3 to the electrolyte, while the current density at this potential achieves about 1 A·cm^{-2} after adding 0.1 M KNO_3, demonstrating the weak competition for HER (Fig. 3(b)). The optimal electrochemical performance of Ce_{10}/CuO is determined by analyzing the LSV curves of Ce_x/CuO across various levels of Ce doping (Fig. S6 in the ESM). Electrochemical impedance spectroscopy (EIS) investigates the interfacial electron transfer kinetics through the measurement of the resistance of the electrodes. The results in Fig. 3(c) suggest that Ce_{10}/CuO exhibits less resistance than CuO in the nitrate reduction reaction, with superior electron transfer capability and electrical conductivity.

Moreover, the activity, selectivity, and economics of the proposed catalysts can be further reflected through quantitative analysis of the products. Amperometric tests for nitrate reduction were first performed at six different potentials (0, –0.1, –0.2, –0.3, –0.4, –0.5 V vs. RHE) (Figs. S7 and S8 in the ESM). The disappearance of the peaks corresponding to CuO in the XRD pattern after the reaction proves that Cu^{2+} is reduced to Cu^0,

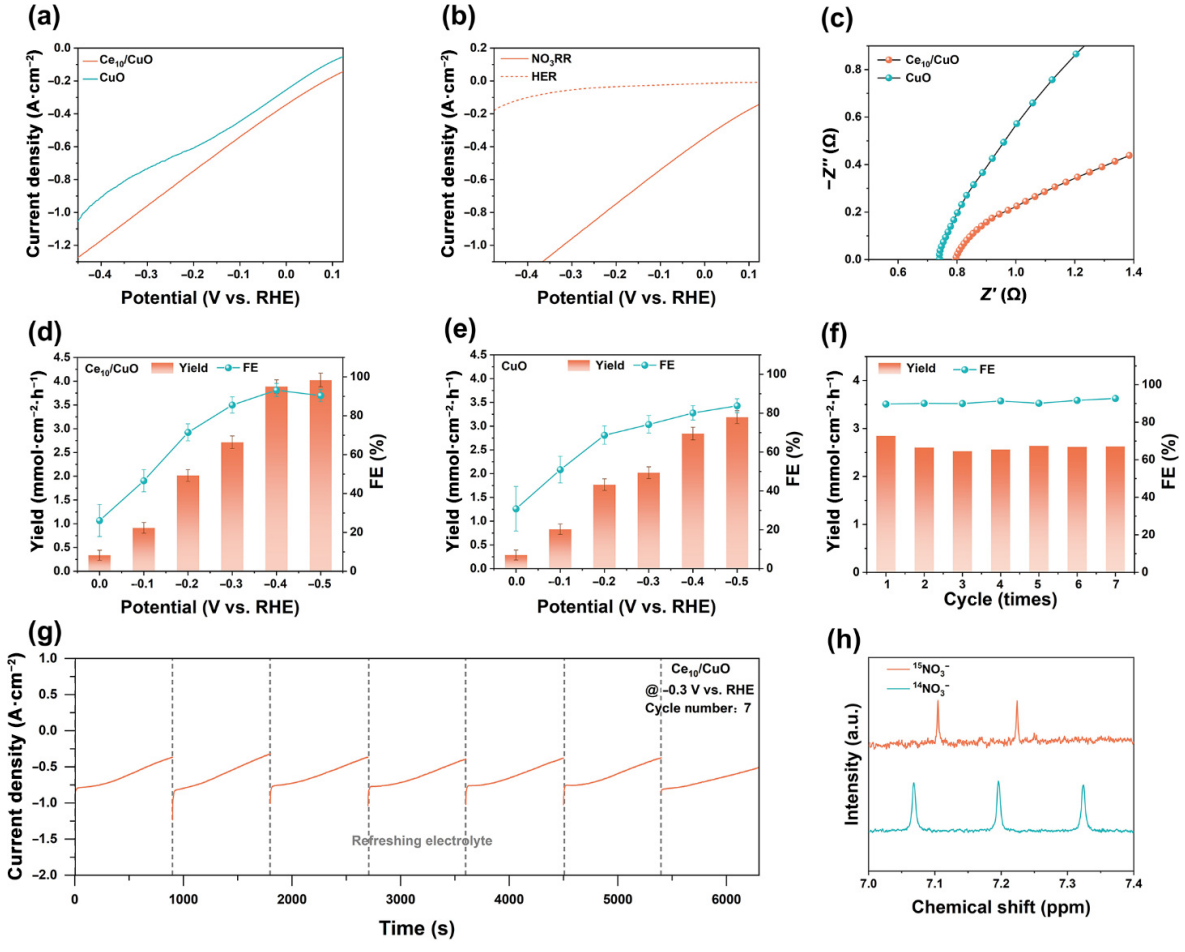

Figure 3 (a) LSV curves of Ce_{10}/CuO (orange) and CuO (blue) in 1 M KOH with 0.1 M KNO_3. (b) LSV curves of Ce_{10}/CuO in 1 M KOH with and without 0.1 M KNO_3. (c) The Nyquist plots over Ce_{10}/CuO and CuO electrocatalysts in 1 M KOH with 0.1 M KNO_3 solution. NH_3 yield and FE of (d) Ce_{10}/CuO and (e) CuO at different potentials. The stability of Ce_{10}/CuO electrocatalyst: (f) NH_3 yield and FE recorded in 1 M KOH with 0.1 M KNO_3 solution under seven cycles; (g) the amperometric tests of nitrate reduction at a constant potential of –0.3 V vs. RHE. (h) ^{1}H NMR spectra of the electrolytes produced from the NitRR using $^{15}NO_3^-$ and $^{14}NO_3^-$.

and Cu^0 species can act as adsorbents and activators of nitrate (Fig. S9 in the ESM) [68]. Figures 3(d) and 3(e) display the NH_3 yields and Faraday efficiencies (FE) of Ce_{10}/CuO and CuO, respectively. The catalyst Ce_{10}/CuO achieves the ammonia yield of 3.88 ± 0.14 mmol·cm^{-2}·h^{-1} at –0.4 V vs. RHE, representing an improvement of 1.04 mmol·cm^{-2}·h^{-1} compared to that of pure CuO (2.84 ± 0.13 mmol·cm^{-2}·h^{-1}). The FE of Ce_{10}/CuO (93.2% ± 3.4%) is about 13% higher than that of CuO (80.1% ± 3.7%). In addition, the FE of CuO at –0.3 V vs. RHE is 74.2% ± 4.5%, which is increased to 85.5% ± 4.1% after Ce doping (Figs. S10–S12 in the ESM). The yield is also raised from 2.01 ± 0.12 to 2.71 ± 0.13 mmol·cm^{-2}·h^{-1}. The yield and FE results demonstrate the remarkable contribution of the introduction of Ce in the nitrate reduction reaction. The parallel incorporation of oxygen vacancies with Ce doping effectively optimized the electronic structure and facilitated the cathodic charge transfer, thus promoting the adsorption of nitrate and hydrogenation to ammonia. NO_2^- is a critical intermediate product in the nitrate reduction reaction process. The accumulation of NO_2^- in the electrolyte will lead to highly toxic NO_2^- covering the surface of the catalyst, thus decreasing the efficiency of ammonia synthesis. Therefore, the content of NO_2^- in the electrolyte was also examined. It shows that the yield of NO_2^- is lower than 14 μmol·cm^{-2}·h^{-1} and the FE is lower than 0.1%, which indicates that little amount of NO_2^- is retained in the electrolyte (Figs. S13 and S14 in the ESM).

The stability of the catalysts and the reproducibility of the ammonia yields are particularly relevant for evaluating their application in practical production. Therefore, several nitrate reduction tests were carried out on Ce_{10}/CuO for seven cycles at –0.3 V vs. RHE. The catalyst exhibits excellent stability, as the ammonia yield is maintained above 2.5 mmol·cm^{-2}·h^{-1} in seven consecutive cycles and all FEs are above 90%, which implies that Ce_{10}/CuO has favorable performance stability throughout the cyclic tests (Figs. 3(f) and 3(g)).

To confirm that the reduction reaction proceeds via nitrate in solution rather than foreign nitrogen sources, ^{15}N isotope labelling experiments were performed. Specifically, isotope labelling experiments were conducted in a gas-tight H-cell under ambient conditions, where the nitrogen from the nitrate ions in the electrolyte (KNO_3) was substituted with the ^{15}N isotope. The reduction products were inspected using 1H nuclear magnetic resonance (NMR) spectroscopy (Fig. 3(h)). The ammonium ion ($^{14}NH_4^+$) in the reaction product shows three peaks at 7.58, 7.17, and 7.31 ppm when $^{14}NO_3^-$ is used as the nitrogen source. Whereas, double peaks attributed to $^{15}NH_4^+$ are observed at 7.10 and 7.23 ppm after switching the nitrogen source from $^{14}NO_3^-$ to $^{15}NO_3^-$. It

indicates that NH_3 is generated from the reduction reaction of nitrate in the electrolyte rather than the foreign nitrogen source.

In situ infrared spectroscopy enables the analysis of water peaks to verify the evolution of active hydrogen in converting nitrate to ammonia. The peaks located within 3110 to 3690 cm^{-1} are attributed to the O–H stretching vibrational modes of the H_2O molecule. The O–H stretching vibrational modes are shown by Gaussian fitting of the spectral peaks to consist of three parts, revealing the presence of three types of water peaks (dangling O–H, tri-H_2O, and tetra-H_2O). By examining the occupancy of the three types of water peaks, the surface condition of the catalyst is more effectively described. Peaks of orange, blue, and yellow for Ce_{10}/CuO and CuO catalysts are ascribed to dangling O–H, tri-H_2O, and tetra-H_2O, respectively (Figs. 4(a) and 4(b)). The occupancies and positions of the three water peaks vary accordingly as the applied voltage is changed. Figure 4(c) displays the peak area ratios of dangling O–H (free H_2O) at different potentials for Ce_{10}/CuO and CuO catalysts. Specifically, the ratios of free water for Ce_{10}/CuO are greater at arbitrary potentials compared to those for CuO. The high-frequency free H_2O adsorbs more easily on the catalyst surface and decomposes to generate active hydrogen since the dangling O–H bond exhibits a weak hydrogen-bonding structure. Therefore, Ce doping facilitates the activation of H_2O on the catalyst surface and contributes to the generation of active hydrogen, which consequently boosts the hydrogenation of nitrate to generate ammonia. The vibration frequency of the adsorbate behaves as a function of the applied electrode potential according to the Stark effect. Figure 4(d) illustrates the magnitude of the wave number variations with applied electrode potential for the three water peaks of Ce_{10}/CuO. With the decrease in potential, the

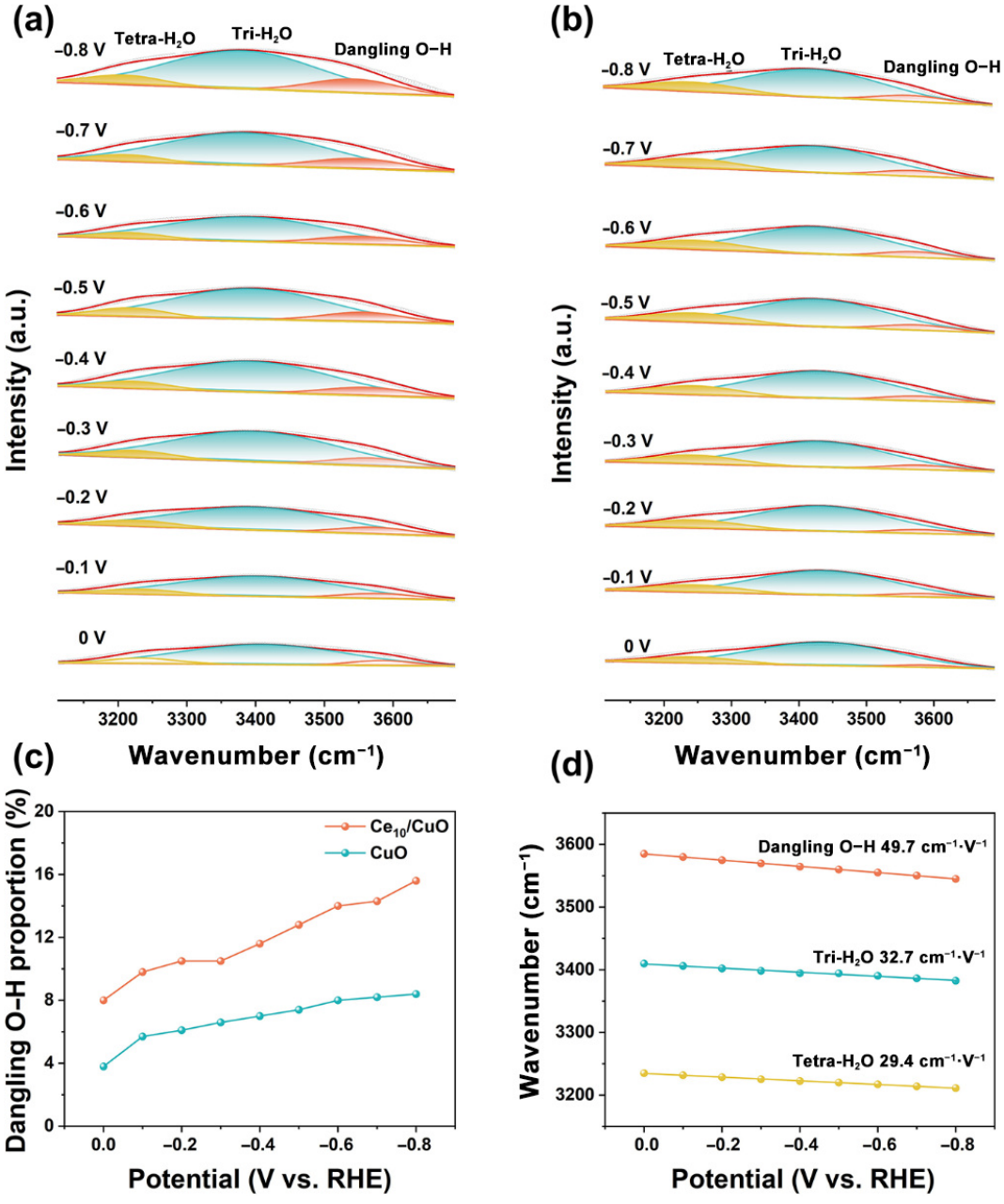

Figure 4 The portion of the *in situ* ATR-SEIRAS of (a) Ce_{10}/CuO and (b) CuO located at 3110–3690 cm^{-1}. (c) The proportion of dangling O–H of Ce_{10}/CuO and CuO catalysts at different potentials. (d) The wavenumber shift of tetra-H_2O, tri-H_2O, and dangling O–H of Ce_{10}/CuO with potential changes.

dangling O–H of Ce_{10}/CuO exhibits a steeper Stark slope (–49.7 $cm^{-1}·V^{-1}$) compared with that of tetra-H_2O (–29.4 $cm^{-1}·V^{-1}$) and tri-H_2O (–32.7 $cm^{-1}·V^{-1}$). This suggests that free H_2O is considerably more sensitive to changes in the applied electric field and that free H_2O of Ce_{10}/CuO dissociates more readily to form active hydrogen.

To achieve insight into the reaction process and mechanism of electrocatalytic nitrate reduction to ammonia, the intermediates were investigated using the attenuated total reflection surface-enhanced infrared absorption spectroscopy (ATR-SEIRAS) technique. Figures 5(a) and 5(b) illustrate the *in situ* infrared spectra of Ce_{10}/CuO and CuO with electrolyte at applied potentials ranging between 0 and –0.8 V vs. RHE. The upward band near 1650 cm^{-1} corresponding to the dissociation of water generates reactive hydrogen that participates in the hydrogenation reaction of $*NO_x$ in solution [68]. The peak intensities in the spectra of Ce_{10}/CuO are significantly stronger than those of CuO at different applied potentials, which further demonstrates that the doping of Ce enhances the dissociation of water. The vibrational band at 1580 cm^{-1} attributed to *NO shows gradual generation of *NO intermediates ranging from –0.1 to –0.4 V vs. RHE [69], followed by gradual consumption for the next steps of the reaction as the potential decreases. The upward band at 1450 cm^{-1} is assigned to the generation of NH^{4+} and the peaks are stronger during catalysis by Ce_{10}/CuO than CuO, which suggests Ce_{10}/CuO may facilitate the conversion of nitrate to ammonia. The decrease in the intensity of the downward band at 1340 cm^{-1} proves the exhaustion of NO_3^- [70, 71]. The gradual enhancement of the upward band at 1120 cm^{-1} demonstrates the formation of NH_2OH. Based on the above results, the following pathway for the nitrate reduction reaction can

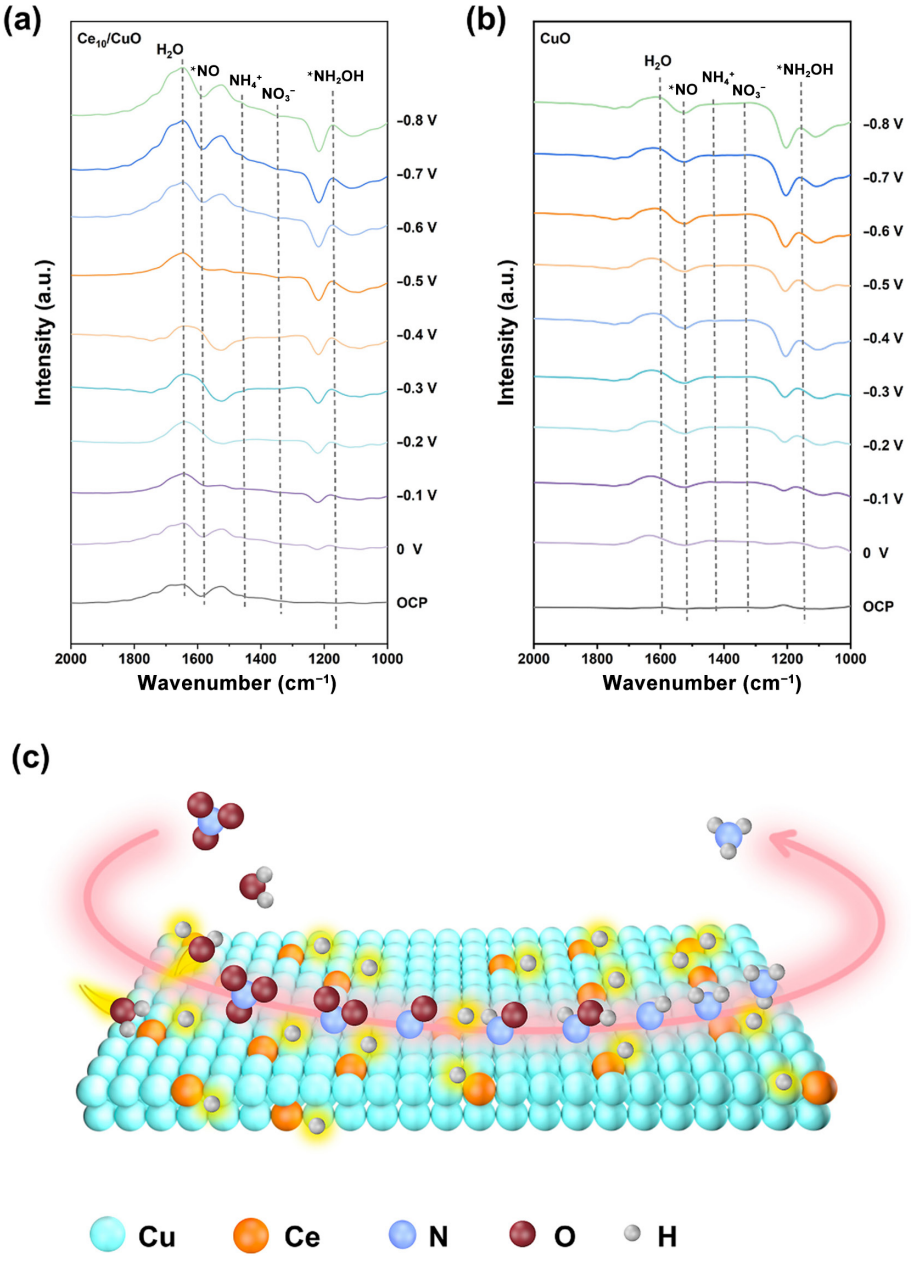

Figure 5 *In situ* infrared spectra of (a) Ce_{10}/CuO and (b) CuO at different potentials, respectively. (c) Mechanism diagram of Ce_{10}/CuO electrocatalytic reduction of nitrate to ammonia.

be inferred: *NO_3 → *NO_2 → *NO → *NH_2OH → *NH → *NH_2 → NH_3 (Fig. 5(c)) [52, 72, 73].

According to the superior nitrate reduction properties of Ce_{10}/CuO, ammonia generation during charging was achieved by assembling a Zn-NO_3^- battery (Fig. 6(a)). Ce_{10}/CuO and Zn foils were applied as the cathode and anode electrodes separately. The anodic electrolyte was 6 M KOH and the cathodic electrolyte was 1 M KOH containing 0.1 M KNO_3. As a result, two batteries connected in series can light up a red light-emitting diode confirming its practical use in energy storage and conversion applications (Fig. 6(b)). The open circuit potential of Ce_{10}/CuO versus Zn^{2+}/Zn is about 1.236 V (Fig. 6(c)). To evaluate the performance of the Zn-NO_3^- battery, the power density was tested. The discharging curve of the Zn-NO_3^- battery is shown in Fig. 6(d), which attains a peak power density of 14.5 mW·cm^{-2} at 38 mA·cm^{-2}. The small peak in the power density curve could be assigned to the transient acceleration or change in the reaction rate, resulting in a significant increase in power output. Furthermore, the output current densities increase as the potential becomes more negative, achieving up to 10, 20, 30, and 40 mA·cm^{-2} at potentials of 0.79, 0.51, 0.36, and 0.21 V vs. Zn^{2+}/Zn, respectively (Fig. 6(e)). Additionally, the electrolytes were removed to detect the products after the discharge tests at different potentials. Figure 6(f) indicates that the NH_3 yield and FE of the Zn-NO_3^- battery gradually rise with the increase of the current density. Specifically, the yield reaches 0.18 mmol·cm^{-2}·h^{-1} with FE of 98.4% at 40 mA·cm^{-2}.

4 Conclusions

In summary, Ce_{10}/CuO prepared by *in situ* oxidative etching and annealing can effectively reduce nitrate to ammonia. The experimental results demonstrate that Ce_{10}/CuO achieves an ammonia yield of 3.88 ± 0.14 mmol·cm^{-2}·h^{-1} at −0.4 V vs. RHE, representing an increase of 1.04 mmol·cm^{-2}·h^{-1} compared to that of CuO, and the FE reaches up to 93.2% ± 3.4%. The excellent electrochemical performance of Ce_{10}/CuO is attributed to the

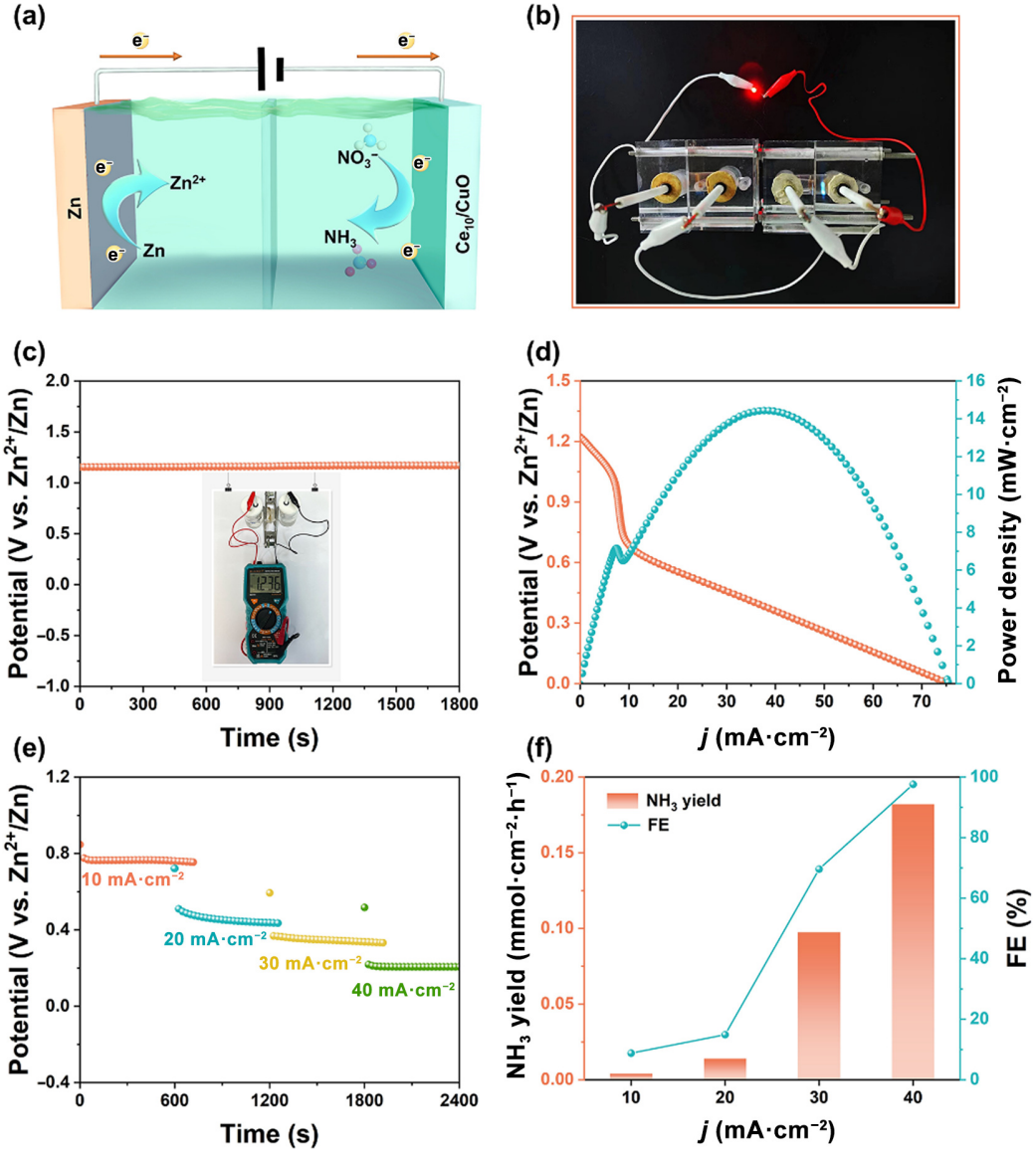

Figure 6 (a) Schematic illustration of Zn-NO_3^- battery. (b) Photograph of a red LED powered by two Zn-NO_3^- batteries using Ce_{10}/CuO. (c) Open circuit potentia (OCP) of Ce_{10}/CuO-based Zn-NO_3^- battery. (d) Discharging curve and the corresponding power density curve of the Ce_{10}/CuO-based Zn-NO_3^- battery. (e) Discharging curves of Ce_{10}/CuO at different current densities. (f) NH_3 yield and FE of Zn-NO_3^- battery with Ce_{10}/CuO catalyst as the cathode.

introduction of Ce^{3+} as a defective indicator that promotes the generation of oxygen vacancies on the catalyst surface and effectively optimizes the electronic structure, which facilitates the adsorption of nitrate and hydrogenation to ammonia. Meanwhile, the free water ratio of Ce_{10}/CuO is greater than that of CuO, which is conducive to the activation of H_2O on the surface of the catalyst and the decomposition of active hydrogen, thus promoting the hydrogenation of nitrate to ammonia. Finally, a Zn-NO_3^- battery with outstanding performance was successfully assembled to achieve a peak power density of 14.5 mW·cm^{-2} at 38 mA·cm^{-2}, which exceeded many reported catalysts.

Electronic Supplementary Material: Supplementary material (information of the experimental procedures and characterization, SEM images, TEM images, UV–Vis absorption spectra, NO_2^- yield and FE of different samples, *I*–*t* curves) is available in the online version of this article at https://doi.org/10.26599/NR.2025.94907135.

Data availability

All data needed to support the conclusions in the paper are presented in the manuscript and the Electronic Supplementary Material. Additional data related to this paper may be requested from the corresponding author upon request.

Acknowledgements

This work was supported by the National Natural Science Foundation of China (Nos. 52072152 and 51802126), the Jiangsu University Jinshan Professor Fund, the Jiangsu Specially-Appointed Professor Fund, Open Fund from Guangxi Key Laboratory of Electrochemical Energy Materials, Zhenjiang "Jinshan Talents" Project 2021, China Post Doctoral Science Foundation (No. 2022M721372), "Doctor of Entrepreneurship and Innovation" in Jiangsu Province (No. JSSCBS20221197), the Postgraduate Research & Practice Innovation Program of Jiangsu Province (Nos. KYCX22_3645 and KYCX24_3964), and Student Research Project of Jiangsu University (Nos. 23A586 and 23A804).

Declaration of competing interest

All the contributing authors report no conflict of interests in this work.

Author contribution statement

J. W. Y.: Data curation, project administration, validation, writing manuscript. Y. L. L.: Data curation, project administration, validation. C. H. F.: Data curation. N. Y. L.: Project administration, funding acquisition. J. Y. Y.: Data curation. Y. X. L.: Writing manuscript, data curation. Y. Y. C.: Validation, data curation. X. Y. Y.: Writing manuscript. X. Y. Z.: Data curation. Y. X. L.: Project administration, writing manuscript. S. J. F.: Writing manuscript. L. X.: Writing manuscript. H. T. L.: Project administration, funding acquisition, writing manuscript. All the authors have approved the final manuscript.

Use of AI statement

None.

References

[1] Yang, W. H.; Chang, Z. W.; Yu, X.; Shen, R. X.; Wang, L. Z.; Cui, X. Z.; Shi, J. L. Triple regulations via Fe redox boosting nitrate reduction to ammonia at industrial current densities. *Angew. Chem., Int. Ed.*, in press, https://doi.org/10.1002/anie.202415300.

[2] Liu, N. Y.; Wu, R. Q.; Liu, Y. X.; Liu, Y. L.; Deng, P. J.; Li, Y. X.; Du, Y. C.; Cheng, Y. Y.; Zhuang, Z. C.; Kang, Z. H. et al. Oxygen vacancy engineering of Fe-doped $NiMoO_4$ for electrocatalytic N_2 fixation to NH_3. *Inorg. Chem.* **2023**, *62*, 11990–12000.

[3] Zhang, Y. Z.; Chen, X.; Wang, W. L.; Yin, L. F.; Crittenden, J. C. Electrocatalytic nitrate reduction to ammonia on defective Au_1Cu (111) single-atom alloys. *Appl. Catal. B* **2022**, *310*, 121346.

[4] Jia, R. R.; Wang, Y. T.; Wang, C. H.; Ling, Y. F.; Yu, Y. F.; Zhang, B. Boosting selective nitrate electroreduction to ammonium by constructing oxygen vacancies in TiO_2. *ACS Catal.* **2020**, *10*, 3533–3540.

[5] Yang, K. W.; Han, S. H.; Cheng, C. Q.; Guo, C. Y.; Li, T. L.; Yu, Y. F. Unveiling the reaction mechanism of nitrate reduction to ammonia over cobalt-based electrocatalysts. *J. Am. Chem. Soc.* **2024**, *146*, 12976–12983.

[6] Zhang, R.; Zhang, Y. Q.; Xiao, B.; Zhang, S. C.; Wang, Y. B.; Cui, H. L.; Li, C.; Hou, Y.; Guo, Y.; Yang, T. et al. Phase engineering of high-entropy alloy for enhanced electrocatalytic nitrate reduction to ammonia. *Angew. Chem., Int. Ed.* **2024**, *63*, e202407589.

[7] Cheng, Y. Y.; Liu, Y. X.; Chu, C.; Liu, Y. L.; Li, Y. X.; Wu, R. Q.; Wu, J. C.; Zhuang, C. Q.; Kang, Z. H.; Li, H. T. Carbon armour with embedded carbon dots for building better supercapacitor electrodes. *Nano Res.* **2023**, *16*, 6815–6824.

[8] Deng, P. J.; Liu, Y. X.; Liu, Y. L.; Li, Y. X.; Wu, R. Q.; Meng, L. J.; Liang, K.; Gan, Y. X.; Qiao, F.; Liu, N. Y. et al. Microwave regenerable nickel, zinc Co-doped nitrogen-coordinated porous carbon catalyst for nitrogen fixation. *ACS Appl. Mater. Interfaces* **2023**, *15*, 44809–44819.

[9] Li, Y. X.; Liu, Y. X.; Liu, X.; Liu, Y. L.; Cheng, Y. Y.; Zhang, P.; Deng, P. J.; Deng, J. J.; Kang, Z. H.; Li, H. T. Fe-doped SnO_2 nanosheet for ambient electrocatalytic nitrogen reduction reaction. *Nano Res.* **2022**, *15*, 6026–6035.

[10] Hao, D.; Liu, Y.; Gao, S. Y.; Arandiyan, H.; Bai, X. J.; Kong, Q.; Wei, W.; Shen, P. K.; Ni, B. J. Emerging artificial nitrogen cycle processes through novel electrochemical and photochemical synthesis. *Mater. Today* **2021**, *46*, 212–233.

[11] Fang, J. Y.; Fan, J. L.; Liu, S. B.; Sun, S. P.; Lou, Y. Y. Copper-based electrocatalysts for nitrate reduction to ammonia. *Materials* **2023**, *16*, 4000.

[12] Liu, Y. L.; Zhuang, Z. C.; Liu, Y. X.; Liu, N. Y.; Li, Y. X.; Cheng, Y. Y.; Yu, J. W.; Yu, R. H.; Wang, D. S.; Li, H. T. Shear-strained Pd single-atom electrocatalysts for nitrate reduction to ammonia. *Angew. Chem., Int. Ed.* **2024**, *63*, e202411396.

[13] Subhadarshini, S.; Pumera, M. Single atom catalyst for nitrate-to-ammonia electrochemistry. *Small*, in press, https://doi.org/10.1002/smll.202403515.

[14] Zhang, H. J.; Fang, K. Q.; Yang, J.; Chen, H.; Ning, J. Q.; Wang, H. Y.; Hu, Y. Strategies and applications of electrocatalytic nitrate reduction towards ammonia. *Coord. Chem. Rev.* **2024**, *506*, 215723.

[15] Zhuang, C. Q.; Chang, Y.; Li, W. M.; Li, S. J.; Xu, P.; Zhang, H.; Zhang, Y. H.; Zhang, C.; Gao, J. F.; Chen, G. et al. Light-induced variation of lithium coordination environment in g-C_3N_4 nanosheet for highly efficient oxygen reduction reactions. *ACS Nano* **2024**, *18*, 5206–5217.

[16] Chen, G. F.; Yuan, Y. F.; Jiang, H. F.; Ren, S. Y.; Ding, L. X.; Ma, L.; Wu, T. P.; Lu, J.; Wang, H. H. Electrochemical reduction of nitrate to ammonia via direct eight-electron transfer using a copper-molecular solid catalyst. *Nat. Energy* **2020**, *5*, 605–613.

[17] Bi, Z.; Zhang, W. J.; Ni, M.; Song, G.; Huang, Y. Fe^0/Fe^{2+}-dependent nitrate reduction in anammox consortia questions the enzymatic

mechanism of nitrate reduction by anammox bacteria. *ACS Sustain. Chem. Eng.* **2020**, *8*, 15278–15287.
[18] Xia, J. K.; Xu, J. W.; Yu, B.; Liang, X.; Qiu, Z.; Li, H.; Feng, H. J.; Li, Y. F.; Cai, Y. J.; Wei, H. Y. et al. A metal-sulfur-carbon catalyst mimicking the two-component architecture of nitrogenase. *Angew. Chem., Int. Ed.* **2024**, *63*, e202412740.
[19] Zhuang, Z. C.; Li, Y.; Li, Z. L.; Lv, F.; Lang, Z. Q.; Zhao, K. N.; Zhou, L.; Moskaleva, L.; Guo, S. J.; Mai, L. Q. MoB/g-C_3N_4 interface materials as a schottky catalyst to boost hydrogen evolution. *Angew. Chem., Int. Ed.* **2018**, *57*, 496–500.
[20] Zhuang, Z. H.; Li, Y.; Li, Y. H.; Huang, J. Z.; Wei, B.; Sun, R.; Ren, Y. J.; Ding, J.; Zhu, J. X.; Lang, Z. Q. et al. Atomically dispersed nonmagnetic electron traps improve oxygen reduction activity of perovskite oxides. *Energy Environ. Sci.* **2021**, *14*, 1016–1028.
[21] Wu, X.; Tong, Z.; Liu, Y. L.; Li, Y. X.; Cheng, Y. Y.; Yu, J. W.; Cao, P.; Zhuang, C. Q.; Shi, Q. Z.; Liu, N. Y. et al. Modification of the CuO electronic structure for enhanced selective electrochemical CO_2 reduction to ethylene. *Nano Res.* **2024**, *17*, 7194–7202.
[22] Hao, J. C.; Zhuang, Z. C.; Cao, K. C.; Gao, G. H.; Wang, C.; Lai, F. L.; Lu, S. L.; Ma, P. M.; Dong, W. F.; Liu, T. X. et al. Unraveling the electronegativity-dominated intermediate adsorption on high-entropy alloy electrocatalysts. *Nat. Commun.* **2022**, *13*, 2662.
[23] Liu, Y.; Xing, Y. Y.; Xu, S. J.; Lu, Y. K.; Sun, S. C.; Jiang, D. L. Interfacing Co_3Mo with $CoMoO_x$ for synergistically boosting electrocatalytic hydrogen and oxygen evolution reactions. *Chem. Eng. J.* **2022**, *431*, 133240.
[24] Dong, W. X.; Zhou, H. B.; Mao, B. D.; Zhang, Z. Y.; Liu, Y. S.; Liu, Y. H.; Li, F. H.; Zhang, D. Q.; Zhang, D. X.; Shi, W. D. Efficient MOF-derived V-Ni_3S_2 nanosheet arrays for electrocatalytic overall water splitting in Alkali. *Int. J. Hydrogen Energy* **2021**, *46*, 10773–10782.
[25] Peng, K.; Bhuvanendran, N.; Ravichandran, S.; Zhang, W. Q.; Ma, Q.; Xing, L.; Xu, Q.; Khotseng, L.; Su, H. N. Carbon supported PtPdCr ternary alloy nanoparticles with enhanced electrocatalytic activity and durability for methanol oxidation reaction. *Int. J. Hydrogen Energy* **2020**, *45*, 22752–22760.
[26] Liu, N. Y.; Liu, Y. X.; Liu, Y. L.; Li, Y. X.; Cheng, Y. Y.; Li, H. T. Modulation of photogenerated holes for enhanced photoelectrocatalytic performance. *Microstructures* **2023**, *3*, 2023001.
[27] Geng, J.; Ji, S. H. Boosting electrocatalytic nitrate reduction to ammonia via $Cu_2O/Cu(OH)_2$ heterostructures promoting electron transfer. *Nano Res.* **2024**, *17*, 4898–4907.
[28] Fan, K.; Xie, W. F.; Li, J. Z.; Sun, Y. N.; Xu, P. C.; Tang, Y.; Li, Z. H.; Shao, M. F. Active hydrogen boosts electrochemical nitrate reduction to ammonia. *Nat. Commun.* **2022**, *13*, 7958.
[29] Zhuang, C. Q.; Li, W. M.; Chang, Y.; Li, S. J.; Zhang, Y. H.; Li, Y. L.; Gao, J. F.; Chen, G.; Kang, Z. H. Coordination environment dominated catalytic selectivity of photocatalytic hydrogen and oxygen reduction over switchable gallium and nitrogen active sites. *J. Mater. Chem. A* **2024**, *12*, 5711–5718.
[30] Liu, Y. X.; Wu, R. Q.; Liu, Y. L.; Deng, P. J.; Li, Y. X.; Cheng, Y. Y.; Du, Y. C.; Li, Z. N.; Yan, X.; Liu, N. Y. et al. Interface engineering of CoS/MoS_2 heterostructure for the electrocatalytic reduction of N_2 to NH_3. *Inorg. Chem. Front.* **2023**, *10*, 5700–5709.
[31] Geng, J.; Ji, S. H.; Xu, H.; Zhao, C. J.; Zhang, S. B.; Zhang, H. M. Electrochemical reduction of nitrate to ammonia in a fluidized electrocatalysis system with oxygen vacancy-rich CuO_x nanoparticles. *Inorg. Chem. Front.* **2021**, *8*, 5209–5213.
[32] Liu, Y. L.; Zheng, Z. Y.; Jabeen, S.; Liu, N. Y.; Liu, Y. X.; Cheng, Y. Y.; Li, Y. X.; Yu, J. W.; Wu, X.; Yan, N. N. et al. Mechanochemical route to fabricate an efficient nitrate reduction electrocatalyst. *Nano Res.* **2024**, *17*, 4889–4897.
[33] Shi, L.; Zhu, H. Y. En route to a circular nitrogen economy. *Nat. Sustain.* **2024**, *7*, 1221–1222.
[34] Wu, Q. F.; Zhu, W. J.; Ma, D. X.; Liang, C.; Wang, Z. C.; Liang, H. F. Screening of transition metal oxides for electrocatalytic nitrate reduction to ammonia at large currents. *Nano Res.* **2024**, *17*, 3902–3910.
[35] Wu, Z. Y.; Karamad, M.; Yong, X.; Huang, Q. Z.; Cullen, D. A.; Zhu, P.; Xia, C.; Xiao, Q. F.; Shakouri, M.; Chen, F. Y. et al. Electrochemical ammonia synthesis via nitrate reduction on Fe single atom catalyst. *Nat. Commun.* **2021**, *12*, 2870.
[36] Wu, Q. L.; Zhu, F. F.; Wallace, G.; Yao, X. D.; Chen, J. Electrocatalysis of nitrogen pollution: Transforming nitrogen waste into high-value chemicals. *Chem. Soc. Rev.* **2024**, *53*, 557–565.
[37] Chen, X. H.; Cheng, Y. M.; Zhang, B.; Zhou, J.; He, S. S. Gradient-concentration RuCo electrocatalyst for efficient and stable electroreduction of nitrate into ammonia. *Nat. Commun.* **2024**, *15*, 6278.
[38] Zhu, W. J.; Zhang, X. Y.; Yao, F.; Huang, R. P.; Chen, Y.; Chen, C. L.; Fei, J. W.; Chen, Y. Q.; Wang, Z. C.; Liang, H. F. A hydrazine-nitrate flow battery catalyzed by a bimetallic RuCo precatalyst for wastewater purification along with simultaneous generation of ammonia and electricity. *Angew. Chem., Int. Ed.* **2023**, *62*, e202300390.
[39] Wen, Y. K.; Wang, T. D.; Hao, J. C.; Zhuang, Z. C.; Gao, G. H.; Lai, F. L.; Lu, S. L.; Wang, X. F.; Kang, Q.; Wu, G. M. et al. A coherent Pd-$Pd_{16}B_3$ core–shell electrocatalyst for controlled hydrogenation in nitrogen reduction reaction. *Adv. Funct. Mater.* **2024**, *34*, 2400849.
[40] Dai, L. J.; Li, S. J.; Dai, Y.; Zheng, Y. J.; Liu, K. H.; Li, H. X.; Jiang, B. Engineering CoO/B heterojunction electrocatalysts for boosting electrocatalytic nitrate reduction to ammonia. *Chem. Eng. J.* **2024**, *498*, 155735.
[41] Zheng, M. Y.; Wan, Y. C.; Yang, L. P.; Ao, S.; Fu, W. Y.; Zhang, Z. J.; Huang, Z. H.; Ling, T.; Kang, F. Y.; Lv, R. T. *In situ* construction of Cu(I)-Cu(II) pairs for efficient electrocatalytic nitrate reduction reaction to ammonia. *J. Energy Chem.* **2025**, *100*, 106–113.
[42] Zhu, W. J.; Yao, F.; Wu, Q. F.; Jiang, Q.; Wang, J. X.; Wang, Z. C.; Liang, H. F. Weakened d-p orbital hybridization in *in situ* reconstructed Ru/β-$Co(OH)_2$ heterointerfaces for accelerated ammonia electrosynthesis from nitrates. *Energy Environ. Sci.* **2023**, *16*, 2483–2493.
[43] Wang, S. W.; Zhuang, Z. C.; Xu, J. W.; Fu, C.; Qiu, Z.; Feng, H. J.; Xiang, H.; Chen, Z. L.; Li, H.; Zhang, L. et al. Non-rigid metal-oxygen bonding empowered nitrate reduction on ruthenium catalysts. *Nano Energy* **2024**, *130*, 110088.
[44] Zheng, S. J.; Dong, X. Y.; Chen, H.; Huang, R. W.; Cai, J. M.; Zang, S. Q. Unveiling ionized interfacial water-induced localized H* enrichment for electrocatalytic nitrate reduction. *Angew. Chem., Int. Ed.*, in press, https://doi.org/10.1002/anie.202413033.
[45] Liu, Z. H.; Du, Y.; Yu, R. H.; Zheng, M. B.; Hu, R.; Wu, J. S.; Xia, Y. Y.; Zhuang, Z. C.; Wang, D. S. Tuning mass transport in electrocatalysis down to sub-5 nm through nanoscale grade separation. *Angew. Chem., Int. Ed.* **2023**, *62*, e202212653.
[46] Zhuang, Z. C.; Xia, L. X.; Huang, J. Z.; Zhu, P.; Li, Y.; Ye, C. L.; Xia, M. G.; Yu, R. H.; Lang, Z. Q.; Zhu, J. X. et al. Continuous modulation of electrocatalytic oxygen reduction activities of single-atom catalysts through p-n junction rectification. *Angew. Chem., Int. Ed.* **2023**, *62*, e202212335.
[47] Zhuang, Z. C.; Li, Y. H.; Yu, R. H.; Xia, L. X.; Yang, J. R.; Lang, Z. Q.; Zhu, J. X.; Huang, J. Z.; Wang, J. O.; Wang, Y. et al. Reversely trapping atoms from a perovskite surface for high-performance and durable fuel cell cathodes. *Nat. Catal.* **2022**, *5*, 300–310.
[48] Yin, S. Y.; Guan, Z. X.; Zhu, Y. C.; Guo, D. Y.; Chen, X. A.; Wang, S. Highly efficient electrocatalytic nitrate reduction to ammonia: Group VIII-based catalysts. *ACS Nano* **2024**, *18*, 27833–27852.
[49] Cheng, Y. Y.; Jabeen, S.; Lei, S. W.; Liu, N. Y.; Liu, Y. X.; Liu, Y. L.; Li, Y. X.; Wu, X.; Tong, Z.; Yu, J. W. et al. N-doped carbon dots-modulated interfacial charge transfer and surface structure in $FeNbO_4$ photocatalysts for enhanced CO_2 conversion selectivity to CH_4. *Chem. Eng. J.* **2024**, *498*, 155576.
[50] Wang, Y. T.; Li, H. J.; Zhou, W.; Zhang, X.; Zhang, B.; Yu, Y. F.

Structurally disordered RuO_2 nanosheets with rich oxygen vacancies for enhanced nitrate electroreduction to ammonia. *Angew. Chem., Int. Ed.* **2022**, *61*, e202202604.

[51] Xu, J. W.; Zhang, S. B.; Liu, H. J.; Liu, S.; Yuan, Y.; Meng, Y. H.; Wang, M. M.; Shen, C. Y.; Peng, Q.; Chen, J. H. et al. Breaking local charge symmetry of iron single atoms for efficient electrocatalytic nitrate reduction to ammonia. *Angew. Chem., Int. Ed.* **2023**, *62*, e202308044.

[52] Bai, L. C.; Franco, F.; Timoshenko, J.; Rettenmaier, C.; Scholten, F.; Jeon, H. S.; Yoon, A.; Rüscher, M.; Herzog, A.; Haase, F. T. et al. Electrocatalytic nitrate and nitrite reduction toward ammonia using Cu_2O nanocubes: Active species and reaction mechanisms. *J. Am. Chem. Soc.* **2024**, *146*, 9665–9678.

[53] Zhang, X.; Wang, Y. T.; Liu, C. B.; Yu, Y. F.; Lu, S. Y.; Zhang, B. Recent advances in non-noble metal electrocatalysts for nitrate reduction. *Chem. Eng. J.* **2021**, *403*, 126269.

[54] Feng, X. T.; Liu, J. Y.; Kong, Y.; Zhang, Z. X.; Zhang, Z. D.; Li, S. Z.; Tong, L. M.; Gao, X.; Zhang, J. Cu/Cu_xO/graphdiyne tandem catalyst for efficient electrocatalytic nitrate reduction to ammonia. *Adv. Mater.* **2024**, *36*, 2405660.

[55] Tong, Z.; Liu, Y. L.; Wu, X.; Cheng, Y. Y.; Yu, J. W.; Zhang, X. Y.; Liu, N. Y.; Liu, X.; Li, H. T. Carbon quantum dots/Cu_2O photocatalyst for room temperature selective oxidation of benzyl alcohol. *Nanomaterials* **2024**, *14*, 212.

[56] Cheng, Y. Y.; Liu, Y. X.; Liu, Y. L.; Li, Y. X.; Wu, R. Q.; Du, Y. C.; Askari, N.; Liu, N. Y.; Qiao, F.; Sun, C. H. et al. A core-satellite structured type II heterojunction photocatalyst with enhanced CO_2 reduction under visible light. *Nano Res.* **2022**, *15*, 8880–8889.

[57] Yan, Q. Y.; Zhao, R. D.; Yu, L. H.; Zhao, Z. Y.; Liu, L.; Xi, J. Y. Enhancing compatibility of two-step tandem catalytic nitrate reduction to ammonia over P-Cu/$Co(OH)_2$. *Adv. Mater.* **2024**, *36*, 2408680.

[58] Hu, Q.; Qin, Y. J.; Wang, X. D.; Wang, Z. Y.; Huang, X. W.; Zheng, H. J.; Gao, K. R.; Yang, H. P.; Zhang, P. X.; Shao, M. H. et al. Reaction intermediate-mediated electrocatalyst synthesis favors specified facet and defect exposure for efficient nitrate-ammonia conversion. *Energy Environ. Sci.* **2021**, *14*, 4989–4997.

[59] Liu, Y.; Huang, S. L.; Lu, J. J.; Niu, S. Y.; Shen, P. K.; Hu, Z. F.; Tsiakaras, P.; Gao, S. Y. $Ni_{0.25}Cu_{0.5}Sn_{0.25}$ nanometallic glasses as highly efficient catalyst for electrochemical nitrate reduction to ammonia. *Adv. Funct. Mater*., in press, https://doi.org/10.1002/adfm.202411325.

[60] Chen, F. Y.; Elgazzar, A.; Pecaut, S.; Qiu, C.; Feng, Y. G.; Ashokkumar, S.; Yu, Z.; Sellers, C.; Hao, S. Y.; Zhu, P. et al. Electrochemical nitrate reduction to ammonia with cation shuttling in a solid electrolyte reactor. *Nat. Catal.* **2024**, *7*, 1032–1043.

[61] Li, Z. L.; Zhuang, Z. C.; Lv, F.; Zhu, H.; Zhou, L.; Luo, M. C.; Zhu, J. X.; Lang, Z. Q.; Feng, S. H.; Chen, W. et al. The marriage of the FeN_4 Moiety and MXene boosts oxygen reduction catalysis: Fe 3d electron delocalization matters. *Adv. Mater.* **2018**, *30*, 1803220.

[62] Zhu, H.; Sun, S. H.; Hao, J. C.; Zhuang, Z. C.; Zhang, S. G.; Wang, T. D.; Kang, Q.; Lu, S. L.; Wang, X. F.; Lai, F. L. et al. A high-entropy atomic environment converts inactive to active sites for electrocatalysis. *Energy Environ. Sci.* **2023**, *16*, 619–628.

[63] Peng, O. W.; Hu, Q. K.; Zhou, X.; Zhang, R. R.; Du, Y. H.; Li, M. Z.; Ma, L.; Xi, S. B.; Fu, W.; Xu, Z. X. et al. Swinging hydrogen evolution to nitrate reduction activity in molybdenum carbide by ruthenium doping. *ACS Catal.* **2022**, *12*, 15045–15055.

[64] Wang, Y. H.; Xu, A. N.; Wang, Z. Y.; Huang, L. S.; Li, J.; Li, F. W.; Wicks, J.; Luo, M. C.; Nam, D. H.; Tan, C. S. et al. Enhanced nitrate-to-ammonia activity on copper-nickel alloys via tuning of intermediate adsorption. *J. Am. Chem. Soc.* **2020**, *142*, 5702–5708.

[65] Fang, J. Y.; Zheng, Q. Z.; Lou, Y. Y.; Zhao, K. M.; Hu, S. N.; Li, G.; Akdim, O.; Huang, X. Y.; Sun, S. G. Ampere-level current density ammonia electrochemical synthesis using CuCo nanosheets simulating nitrite reductase bifunctional nature. *Nat. Commun.* **2022**, *13*, 7899.

[66] Zhang, S.; Wu, J. H.; Zheng, M. T.; Jin, X.; Shen, Z. H.; Li, Z. H.; Wang, Y. J.; Wang, Q.; Wang, X. B.; Wei, H. et al. Fe/Cu diatomic catalysts for electrochemical nitrate reduction to ammonia. *Nat. Commun.* **2023**, *14*, 3634.

[67] Zhang, Y. Y.; Hai, G. T.; Huang, Z. S.; Liu, Z. M.; Huang, X. B.; Wang, G. Ce-doping rather than CeO_2 modification and their synergistic effect: Promotion from Ce species in the electrocatalytic oxidation of 5-hydroxymethylfurfural over NiFe-LDH. *Adv. Energy Mater.* **2024**, *14*, 2401449.

[68] Jang, W.; Oh, D.; Lee, J.; Kim, J.; Matthews, J. E.; Kim, H.; Lee, S. W.; Lee, S.; Xu, Y.; Yu, J. M. et al. Homogeneously mixed Cu-Co bimetallic catalyst derived from hydroxy double salt for industrial-level high-rate nitrate-to-ammonia electrosynthesis. *J. Am. Chem. Soc.* **2024**, *146*, 27417–27428.

[69] Guo, X. T.; Yu, J. D.; Ren, S. J.; Gao, R. T.; Wu, L. M.; Wang, L. Controlled defective engineering on CuIr catalyst promotes nitrate selective reduction to ammonia. *ACS Nano* **2024**, *18*, 24252–24261.

[70] Hao, J. C.; Wang, T. D.; Yu, R. H.; Cai, J.; Gao, G. H.; Zhuang, Z. C.; Kang, Q.; Lu, S. L.; Liu, Z. H.; Wu, J. S. et al. Integrating few-atom layer metal on high-entropy alloys to catalyze nitrate reduction in tandem. *Nat. Commun.* **2024**, *15*, 9020.

[71] Liu, H. W.; Yang, C. J.; Dong, C. L.; Wang, J. S.; Zhang, X.; Lyalin, A.; Taketsugu, T.; Chen, Z. Q.; Guan, D. Q.; Xu, X. M. et al. Electrocatalytic ammonia oxidation to nitrite and nitrate with NiOOH-Ni. *Adv. Energy Mater.* **2024**, *14*, 2401675.

[72] Shi, L.; Li, Y. M.; He, S. X.; Liu, Y. N.; Tang, X. Y.; Ao, L.; Lv, X. S.; Fu, W. Y.; Jiang, G. M. Efficient electrocatalytic nitrate reduction on molecular catalyst with electron-deficient single-atom $Cu^{\delta+}$ sites. *Chem. Eng. J.* **2024**, *495*, 153427.

[73] Hao, J. C.; Wang, T. D.; Cai, J.; Gao, G. H.; Zhuang, Z. C.; Yu, R. H.; Wu, J. S.; Wu, G. M.; Lu, S. L.; Wang, X. F. et al. Suppression of structural heterogeneity in high-entropy intermetallics for electrocatalytic upgrading of waste plastics. *Angew. Chem*., in press, https://doi.org/10.1002/ange.202419369.